## PAPER

Check for updates

# Thermodynamic stability screening of IR-photonic processed multication halide perovskite thin films†

Sandy Sánchez, [ID] *[ab] Brian Carlsen,[a] Viktor Škorjanc, [ID] [a] Natalie Flores, [ID] [a] Patricio Serafini,[d] Iván Mora-Seró, [ID] [d] Pascal Schouwink,[c] Shaik M. Zakeeruddin,[b] Michel Graetzel[b] and Anders Hagfeldt [ID] [ae]

We report a material screening study for phase transitions of multication hybrid halide perovskite films. Two hundred sixty-six films processed with flash infrared annealing were optically and structurally characterized. This data was compiled into a database to use as a reliable guide for fundamental studies of halide perovskites. We determine the optimum conditions for the formation of the mixed-cations halide perovskite active phase. We subjected the films to different stress conditions (light, temperature, humidity) resulting in five compositions that were thermodynamically stable. From these, the photoinduced phase instability process of the hybrid perovskite films was explored. These intrinsic stability tests showed that the correct multication combination plays a fundamental role in the crystal growth and thermodynamic stability of the films.

## 1. Introduction

Perovskite solar cells (PSC) have now achieved efficiencies above 25%,[1,2] approaching the record for monocrystalline silicon.[3–5] However, while efficiencies soar, new fabrication methods have remained on the ground. From the lab to commercial scale, this leaves a vast opening for perovskites to evolve.[6–8] With machine learning techniques able to predict material properties ever more quickly, there is a growing need for fast fabrication methods that allow these predictions to be experimentally verified.[9–11] To this end, we used our in-house developed thin film annealing technique called Flash Infrared Annealing (FIRA) to rapidly process thin-film layers[12–15] without using an antisolvent step. FIRA has shown an enormous potential for upscaling PSCs, reducing dramatically the environmental impacts when compared with traditional solution processed PSCs including antisolvent steps and thermal annealing.[13] We then used the Thot data analysis package to quickly integrate and analyze our results. Using these technologies in tandem allowed us to rapidly process a large number of halide perovskite thin films with different cation stoichiometry, screening them for the most stable perovskite compositions.

Two hundred sixty-six perovskite films were deposited on FTO using FIRA processing to anneal them. The 266 samples are composed of 14 different recipes, each of which was processed using 19 different annealing times. Each film required approximately 20 seconds[9,10] to be fully processed, including spin-coating and annealing, making the total processing time roughly two hours.[15,16] Each sample was then characterized simultaneously with optical imaging and absorption spectroscopy, and later with Fourier transform infrared spectroscopy (FTIR) and X-ray diffraction (XRD). A database containing these results is available as a guide for others to use in their studies of perovskite (see Datasets). After rapid screening of the initial 266 films, the most promising in terms of photoconversion performance were chosen for further analysis in regards to their stability.

The ten most stable films were subjected to isolated stress tests of temperature, humidity, and illumination. Only the illumination stressed films showed signs of perovskite phase instability, pointing to photoinduced $PbI_2$ degradation as the cause. As elucidated in recently reported models, a polaron – an electron–phonon coupling during illumination – can render phase separation thermodynamically favorable at a point defect.[17–19] These models are widely reported for segregated phases in mixed halide perovskite compositions, however, from a thermodynamic point of view, under light exposure perovskite phase instabilities undergo lattice deformation with different activation energies.[20] Lattice deformations, likely localized in different spatial regions, ease polaron formation and stabilize

*[a]Laboratory of Photomolecular Sciences, Institute of Chemistry and Chemical Engineering, École Polytechnique Fédérale de Lausanne, 1015 Lausanne, Switzerland. E-mail: sandy.sanchezalonso@epfl.ch; anders-hagfeldt@uu.se*

*[b]Laboratory of Photonics and Interfaces, Institute of Chemistry and Chemical Engineering, École Polytechnique Fédérale de Lausanne, 1015 Lausanne, Switzerland*

*[c]Institute of Chemical Sciences and Engineering, École Polytechnique Fédérale de Lausanne (EPFL), 1950 Sion, Switzerland*

*[d]Institute of Advanced Materials (INAM), Universitat Jaume I, Av. Sos Baynat, s/n, 12071 Castelló, Spain*

*[e]Department of Chemistry – Ångström Laboratory, 5, Uppsala University, Box 523, SE-751 20 Uppsala, Sweden*

† Electronic supplementary information (ESI) available. See DOI: 10.1039/d1ta05248a

This journal is © The Royal Society of Chemistry 2021

*J. Mater. Chem. A*, 2021, **9**, 26885–26895 | **26885**

electrons and holes.[19,21–23] F. Zheng et al. studied large polaron formation with a polarization effect as a cause of cation molecule rotation, and the thermal vibration of the $PbI^{-3}$ sublattice.[22] L. Zhou et al. reported that cation mixtures reduce the bonding energies of small polarons for electrons and holes by approximately a factor of two compared to pure $MAPbI_3$, and to a lesser extent compared to $CsPbI_3$ and $FAPbI_3$.[22,24]

Photoinduced phase segregation processes in mixed halide perovskite, such as ion diffusion through the perovskite lattice, are known to give rise to film degradation.[25] As a cause of the polaronic effect, Hoke et al. indicated that light soaking causes segregation into two crystalline phases after observing the formation of luminescent trap states in perovskite films.[26] Slotcavage et al. proposed that this phase segregation is affected by lattice strain under illumination, which modifies the local perovskite composition.[26,27] Limmer and Ginsberg showed that spontaneous phase separation under steady-state illumination conditions depends not only on morphology, but also strongly on composition and thermodynamic state.[28] They postulate that specific defect structures lead to local modulation of an existing miscibility phase transition in the presence of excess charge carriers. Both Bischak and Ginsberg proposed that localized strain induced by an electron–phonon coupling can promote phase separation.[29]

Exposure to light is one of the main causes of mixed halide perovskite segregation and mixed cation perovskite instabilities (our study) phenomena. These degradation processes can be mitigated by increasing the lattice's stiffness and reducing the number of defects, which can be achieved through smart compositional design and processing.[20,30–35] Jinlu He et al. demonstrated that nonradiative electron–hole recombination is reduced in methylammonium lead iodide ($MAPbI_3$) doped with

formamidinium (FA) and guanidinium (GA) cations because the crystal lattice stiffens, causing the electron–phonon coupling to decrease.[36] More recently, Rachel E. Beal et al. found that Cs substitution improves crystallinity and stabilizes mixed halide perovskites against photoinduced phase segregation.[37] They argue that no cubic material is stable to phase segregation, while some cubic–tetragonal mixed phase materials are stable. However, photoinduced phase segregation is a complex phenomenon, which requires further experimental investigations to be fully understood.[33,38–40]

During crystal growth, vacancy and interstitial point defects, among others, create sub-band gap states and deep traps which act as recombination centers and enable ion migration.[41,42] Reducing the density of these defects will improve the stability.[36,43,44] Therefore, in this work, we investigate an optimized processing and material design for obtaining thermodynamically stable perovskite compositions, and to mitigate the formation of defects during crystal growth.[45–48] We designed a rapid screening process using FIRA to quickly fabricate perovskite films, and used it to determine the best processing and stoichiometric parameters. The ten best films were chosen for stability analysis, which revealed that photodecomposition is the main contributor to the samples' $PbI_2$ degradation.

## 2. Material screening: results and discussion

Two hundred sixty-six hybrid perovskite thin films were annealed using FIRA (see Method's section, experimental conditions are summarized in Table S1†). The general formula of the films is $(FA_xCs_yMA_z)PbI_3$, where $0.80 \leq x \leq 0.95$, $0.05 \leq y \leq 0.20$, and $z = 1 - x - y$, and where FA and MA are



**Fig. 1** Film evolution during annealing. Optical images are measured in transmission mode. Optical absorption spectra, and FTIR measurement were performed on a single spot for $FA_{0.85}MA_{0.1}Cs_{0.05}PbI_3$ perovskite composition and three flash times.

**26886** | J. Mater. Chem. A, 2021, **9**, 26885–26895

This journal is © The Royal Society of Chemistry 2021

formamidinium and methylammonium respectively. We first screened the materials to find the most thermodynamically stable compositions. For this purpose, we used Thot, a data analysis and management tool that allowed us to quickly integrate and analyze our data. We further analyzed the stable compositions and verified our findings by replacing $I^-$ with $Br^-$ as the halide and $Pb^+$ with $Sn^+$ as the metal cation.

Optical image and UV/vis absorption measurements were performed simultaneously directly after film preparation, after which an FTIR spectrum was measured (in the same measured spot). An example of these measurements for a single composition at three different flash times $t_f$ (IR irradiation time) are shown in Fig. 1 with more examples in Fig. S1.† The optical images and the absorption spectra display the evolution of grain formation with increasing annealing time. The sample prepared with $t_f = 0.4$ s flash time shows growth of dendritic formations from nucleation centers.[49] There is no absorption in

the visual range, indicating unreacted mixed species and underdeveloped grains. The image of the sample at $t_f = 1.4$ s, shows a phase transition to perovskite evidenced by the formation of a compact microarray of grain domains and the appearance of an optical bandgap near 1.5 eV.[48,50] In the image of the sample with $t_f = 3.4$ s, signs of perovskite film degradation appear: the grain boundaries are no longer entirely distinguishable, which may be due to thermal evaporation of the organic cations, and there is again no optical absorption in the visual spectra.[51–53]

In the FTIR spectra from Fig. 1 we focused our attention to the absorbance peaks related to the frequency of vibrational modes of the organic cation with wavenumber from $10^3$ to $2 \times 10^3$ cm$^{-3}$. These show an evolution of the cation-associated vibrational transition dipole moment. The peak at $(1713 \pm 2)$ cm$^{-1}$ reflects the FA cation's strong C–N antisymmetric stretching vibration, resulting from hydrogen bonding to the
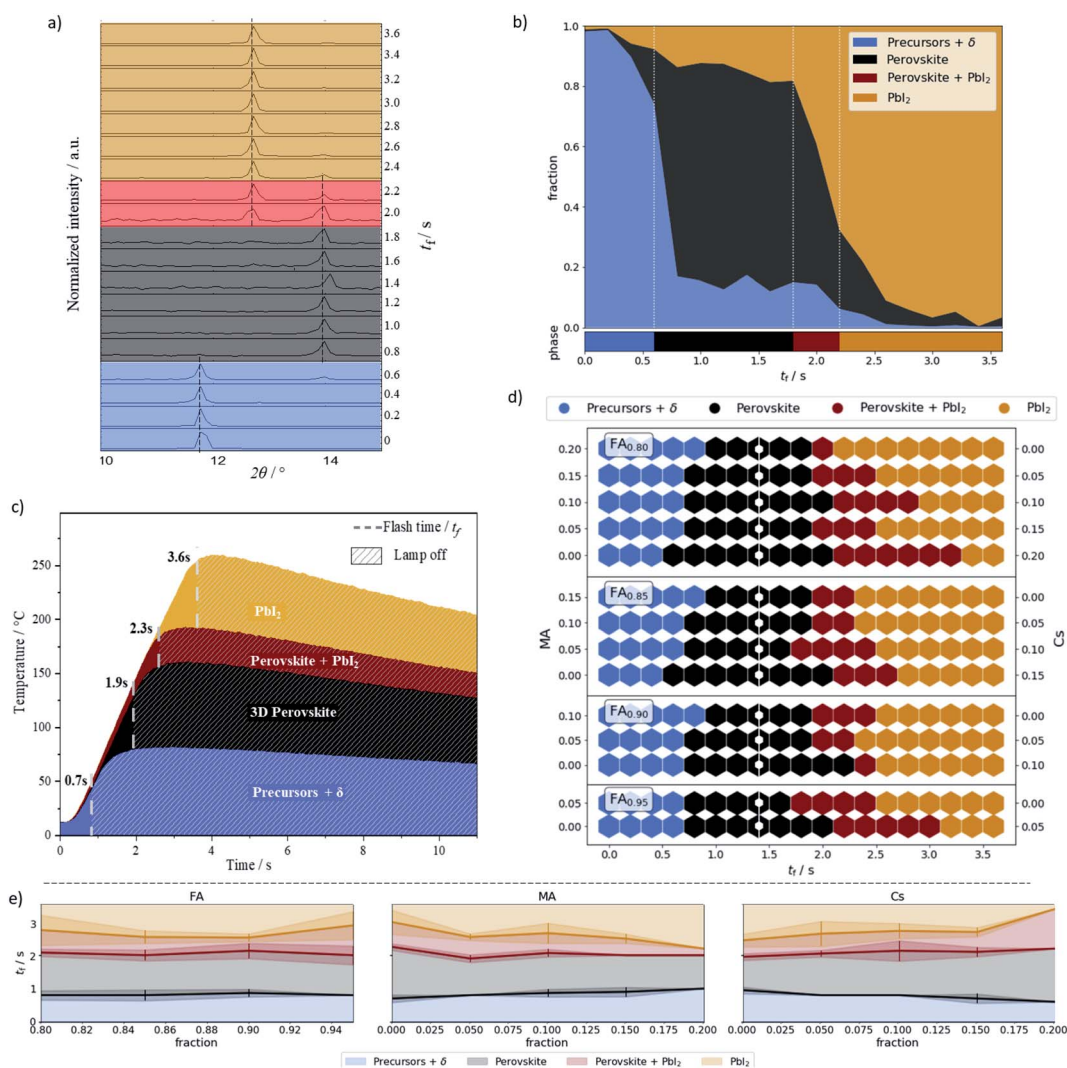


**Fig. 2** (a–c) show results for composition $FA_{0.85}MA_{0.1}Cs_{0.05}PbI_3$. (a) XRD pattern and phase assignment. (b) Fraction of peak heights for different flash times $t_f$ and the corresponding phase classification. (c) Temperature profile as a function of the annealing time and the assigned phases. (d) Assigned phase for each composition as a function of flash time. White dots mark samples at the optimal annealing time (1.4 s). (e) Phase transition for cation ratio fractions with a standard deviation error bar.

This journal is © The Royal Society of Chemistry 2021

*J. Mater. Chem. A*, 2021, **9**, 26885–26895 | **26887**

lead iodide octahedra of the perovskite phase.[54,55] It is present in the spectrum of the $t_f = 1.4$ s sample, and correlates with the high ratio of perovskite present in the film – the cations diffused into the lead iodide cage forming a 3D perovskite network. On the contrary, the absence of this peak for the $t_f = 0.4$ s sample is due to the fact that the perovskite phase has not yet formed, and for the $t_f = 3.4$ s sample due to phase separation of the organic cation as indicated by the XRD patterns available in Datasets. The phase separation is caused by the high temperature (almost 250 °C, Fig. S2†), leading to a change of film color from black to yellow, which is strong evidence of $PbI_2$ phase predominance.

XRD analysis was performed on all 266 samples (see Methods†). The ratio of the peak heights at 11.6, 12.7, and 14.0 $2\theta$ degrees – $FAPbI_3$ based $\delta$ phase, $PbI_2$, and perovskite phases, respectively – was used to assign the percentage of each phase within the material (Datasets). Note that the assigned $\delta$ phase is based on the peak position-identification of the XRD patterns (see Fig. S3†),[56,57] where unreacted materials (precursors) are coexisting with polyforms non-perovskite phases. Overall, this criterion can be used for a rough phase identification.[55,58–60] Fig. 2a shows the XRD pattern and classification for each annealing time of a single sample, namely $FA_{0.85}MA_{0.1}Cs_{0.05}PbI_3$. The phase assignment of this sample is shown in Fig. 2b, and phase assignments for all samples are shown in Fig. 2d. Plots for all the samples can be found in Datasets. In Fig. 2b, the main plot shows the fraction of each phase as a function of annealing time, while the bar underneath shows the phase classification.

A sample was classified as "precursor + $\delta$" if the $\delta$ phase peak ($2\theta = 11.6°$) was higher than both perovskite and $PbI_2$ peak. Otherwise, a ratio between perovskite and $PbI_2$ peak was calculated. If this ratio was above 0.75 the sample was classified as perovskite, if the ratio was between 0.75 and 0.20 it was classified as a mixed perovskite/$PbI_2$ phase, and if the ratio was below 0.20 it was classified as $PbI_2$. These designations are summarized in Table 1. The 0.75 and 0.20 ratios were empirically chosen to give a contiguous sequence of phase classifications. For example, choosing a ratio of 0.8 creates isolated mixed phase classification assignments.

FIRA provides the phase transition energy in a thermal form. A powerful IR radiation source is used for annealing, heating the sample at a rate of 50 °C per second. Fig. 2c shows the temperature profiles of the representative annealing times, i.e. the median annealing times at which the classification changes. All the profiles can be seen in Fig. S4† and more information is detailed in other technical reports.[15,16]

Examining Fig. 2d gives insight into the phase transitions for each composition. Higher Cs-content – moving down in each group – allows the material to withstand longer annealing times before degrading into $PbI_2$. The annealing time to enter the perovskite classification is quite broad and remains relatively constant across all the compositions. The median time in the perovskite classification is 1.4 s, which we take to be the optimal flash time.

In addition to the thermal energy provided by FIRA, a small contribution of energy to the phase transition can also be attributed to chemical forms of energy. To understand this contribution, an analysis of transition phases as a function of a single cation fraction is shown in Fig. 2e. For FA variation, there is almost no dependence on the transition from the precursor to perovskite classification. However, there is a dependence on the MA and Cs amounts. These are intrinsically inversely proportional as the composition space has only two degrees of freedom, the fraction of the Cs being fully determined by MA and FA. The faster transition times for the high Cs content material show that less thermal energy is required to initiate the phase transition. This indicates a faster kinetic reaction pathway to form the perovskite phase, and allows significant control of the structural transition through intermediate phases.[61,62] The volatility of MA also becomes apparent when examining the transition to the $PbI_2$ classification, where a higher MA concentration leads to perovskite decomposition at an earlier time.[63,64]

We analyzed in more detail each of the 14 compositions annealed at the optimal time, $t_f = 1.4$ s, that crystallize in the perovskite phase. Fig. 3a shows optical images of the films' microstructured grain–domains and Fig. S5† shows the absorption spectra for all of them. The microarray domains show inter-boundary gaps, seen clearly in the zoom-in images, for the Cs-free, i.e. $X = 0$, compositions. The area fraction of the gaps for these samples are seen in Fig. 3b. When Cs is present, the films become compact, creating gap-free domains. These gaps are likely due to the high MA content, resulting in different growth rates of the dendrites during formation and different thermal activation energies necessary for the perovskite phase.[14,65] An isotropic growth velocity of the dendrites is crucial to remove defects and form a homogeneous and compact film, which also prevents the formation of secondary phases.[15,59] This is bolstered by the results presented in Fig. 2e, which show the lower thermal activation energy of the perovskite phase with higher Cs content.

From the 14 samples analyzed above we disregarded the Cs-free samples due to the inter-boundary gaps and further analyzed and stress tested the ten remaining samples. The XRD spectra of these samples were analyzed in more detail, as shown in Fig. 4a and b. The Bragg reflections of (001) at 13.9° and (002) at 27° $2\theta$ angles, characteristic of the perovskite phase, are present in the patterns of all the samples. The lattice parameters are extracted from a refinement of the XRD patterns with a profile fit and the refinement parameters of composition $FA_{0.8}MA_{0.05}Cs_{0.15}PbI_3$ were fixed for a displacement free calculation of the rest of the samples (see Methods†). The fit indicates there are no secondary phases present in any of the

**Table 1** Classification rules for phase identification

| Peak ratio\classification | Precursors + $\delta$ phase | Perovskite | Perovskite + $PbI_2$ | $PbI_2$ |
|---|---|---|---|---|
| $\delta$ phase | Tallest | — | — | — |
| Perovskite/$PbI_2$ | — | >0.75 | 0.20–0.75 | <0.20 |

26888 | J. Mater. Chem. A, 2021, 9, 26885–26895

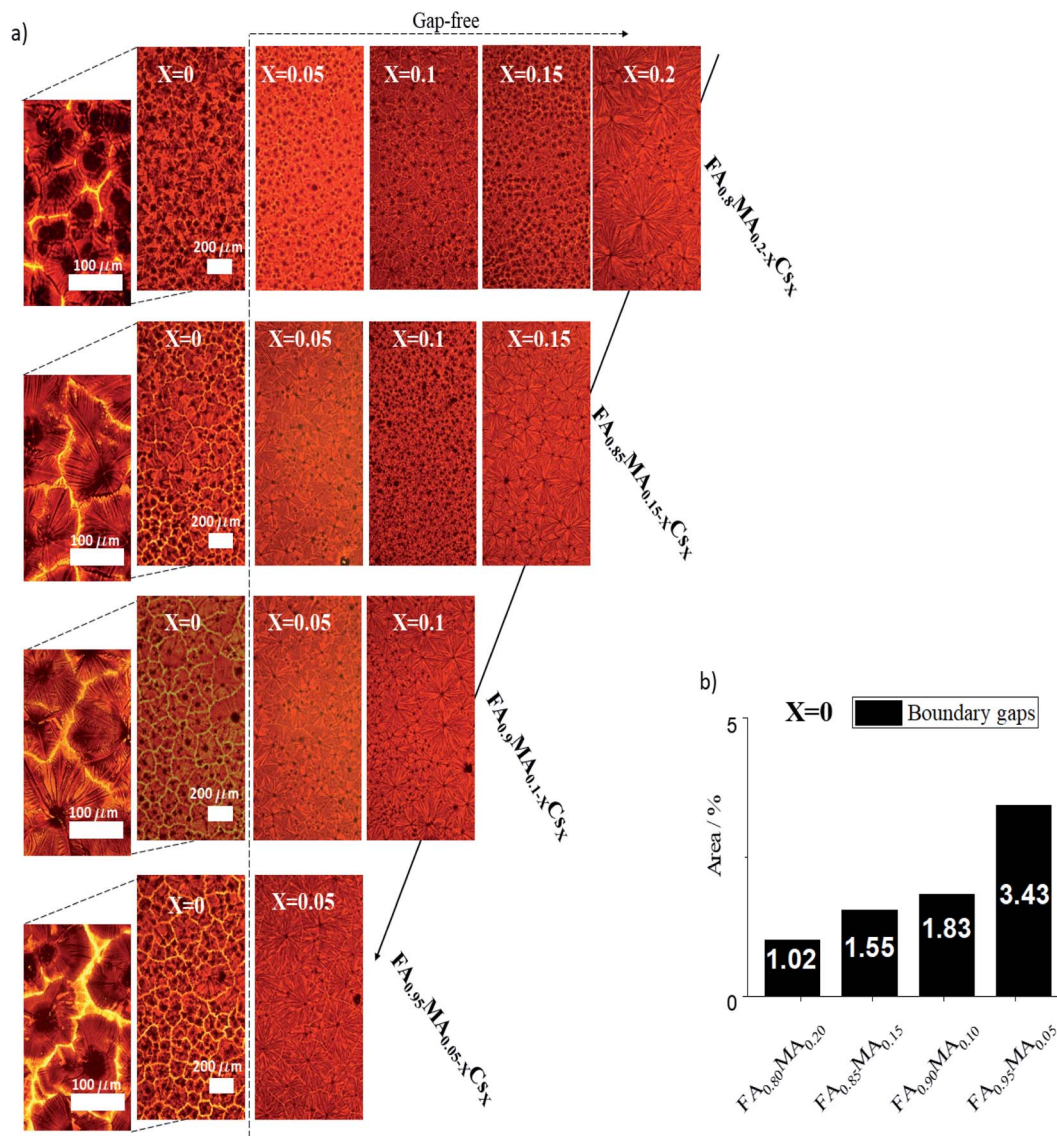This journal is © The Royal Society of Chemistry 2021

Fig. 3  (a) Optical images of the fourteen selected perovskite films. (b) Area percent of gaps with respect to grain domains for the Cs-free films.

samples (see Table S2 and Methods†). The chart of Fig. 4b shows the unit cell volume fraction $V_f$ of the selected films. For the 80% FA compositions there is not a clear trend in terms of lattice expansion or contraction as the MA : Cs stoichiometry changes. This may be due to the exclusion of the Cs and MA cations in the lattice.[26] However, the volume changes within the 85% and 90% FA groups, matching the ionic radius of the MA : Cs ratio, suggest the cations are integrated in the perovskite lattice. From the 85% to the 95% FA group-compositions there is an average increase of the $V_f$ as a function of the different cation ratios, confirming a high accuracy of the lattice parameters calculated from the refinement and reported elsewhere.[66-68]

These ten compositions were then subjected to three stress tests for 200 hours: (1) a relative humidity of 80%, (2) a temperature of 100 °C, and (3) 1 sun illumination. The temperature and illumination tests were performed in an inert atmosphere.

Afterward, XRD was measured for each sample and compared with the initial for structural and phase analysis. These are shown in Fig. S6.† The appearance of a peak at $(12.7 \pm 0.1)$ $2\theta$ indicates that $PbI_2$ has formed as a secondary phase, and there is no evidence that any of the stressed samples showed the δ phase. If the height ratio of the $PbI_2$ to perovskite peak was more than 0.1, the film was classified as degraded. Fig. 4c compares $PbI_2$ degradation for the three stress conditions per composition, where the red frames denote degraded films, and Fig. S7† shows the degradation evolution within each FA group. Notice that $PbI_2$ degradation only appears under the 1-sun illumination stress test; all ten films were stable under both 80% relative humidity and 100 °C for the 200 hour duration of the tests. Finally, time-resolved PL was measured for the five most stable samples under illumination, showing a long charge-carrier lifetime of between 100 to 180 ns and comparable to that reported in the literature,[69-72] as shown in Fig. S8 and Table S3.†
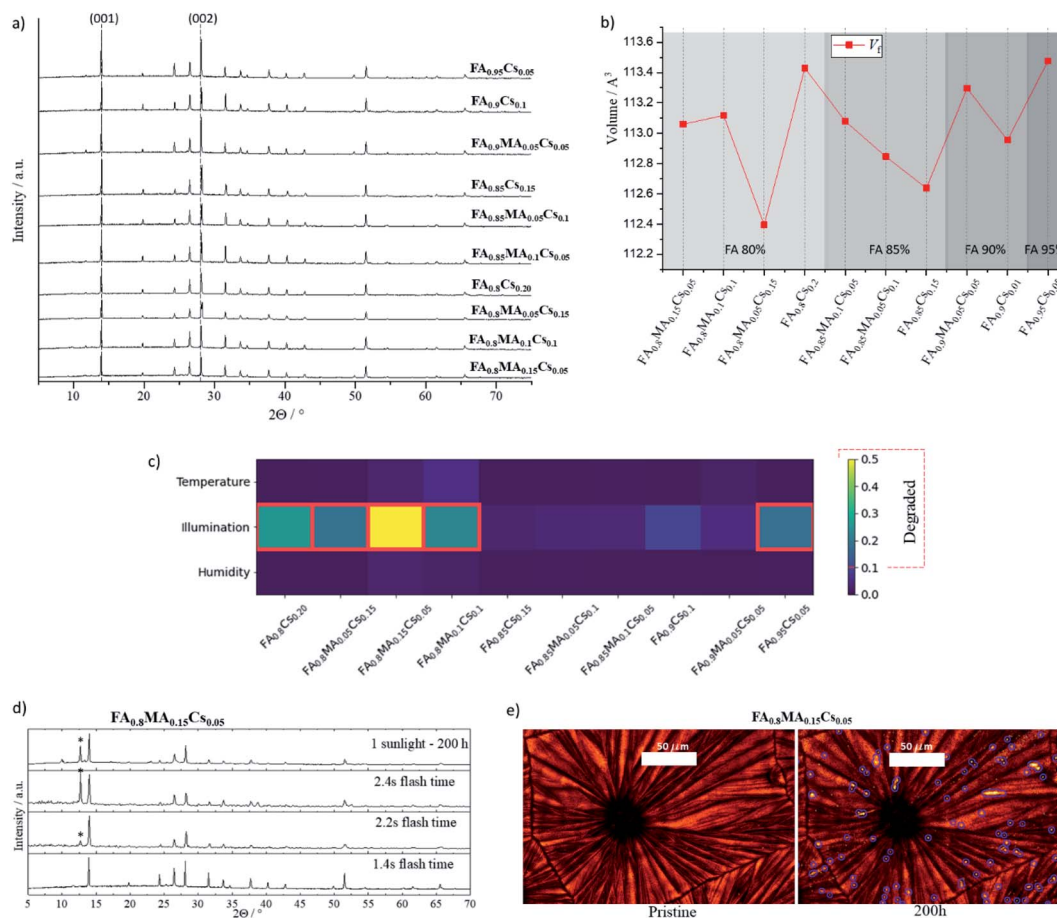
This journal is © The Royal Society of Chemistry 2021

*J. Mater. Chem. A*, 2021, **9**, 26885–26895 | **26889**

Fig. 4 (a) XRD pattern of the ten pristine films. (b) Unit cell volume $V_f$ of the 3D perovskite of the selected films. (c) Relative $PbI_2$ peak height compared to the perovskite peak. Red boxes indicate films classified as degraded. (d) XRD patterns of the $FA_{0.8}MA_{0.15}Cs_{0.05}$ film for 1.4 s, 2.2 s, and 2.4 s flash time and 1.4 s illumination stressed film (the marked Bragg reflection with an asterisk denotes the presence of $PbI_2$ phase). (e) Optical image of the $FA_{0.8}MA_{0.15}Cs_{0.05}$ film before and after the illumination stress test. Microdots are outlined in blue.

In Fig. 4d, XRD patterns from the illumination-stress tested sample and over-annealed samples at 2.2 s and 2.4 s are compared with the sample annealed at the optimal time. Both the over-annealed samples and the stressed sample show a similar change in the pattern, indicating the presence of $PbI_2$. This points to comparable degradation mechanisms being present for the thermal (IR irradiation) and photoinduced stress. As discussed before, Ginsberg's electron–phonon coupling model shows that a high concentration of defects within halide perovskite can facilitate ion diffusion leading to phase segregation due to a polaronic effect.[73,74] Their model argues that polaron formation generates sufficient strain to allow thermodynamically favorable local phase segregation. On the other hand, a polaron binding energy can be tuned by mixing cations in perovskite halides, as investigated in topical studies.[24,75–77] Therefore, the polaronic effect as a major degradation phenomenon, involving halide segregation and phase decomposition, can be facilitated by inhomogeneities during crystal growth, e.g. for the most unstable stoichiometries presented in this work.[24,78–80] Thermally induced lattice strain can also emerge above the perovskite phase transition temperature (Fig. 2c), which leads to ion diffusion and $PbI_2$ degradation;

however, optimizing the cationic site stoichiometry and improving crystallinity can mitigate the entropy of thermal and photoinduced decomposition mechanisms.[81–83] This is in agreement as well with a theoretical report led by Wei Jian et al., where $Cs^+$ can stabilize the inorganic framework in hybrid perovskite halide materials at room temperature.[84]

Fig. 4e presents optical images of the pristine and 1-sun stressed sample $FA_{0.8}MA_{0.15}Cs_{0.05}PbI_3$. The degradation of this high-content MA material is evident in the microdots visible in the images after 200 hours. Fig. S9† shows an expanded image characterization for the studied film compared with the most stable composition $FA_{0.9}Cs_{0.1}PbI_3$ with absorption spectra. The surface temperature of the samples was controlled to ensure thermal effects would not cause degradation by keeping it at 35 °C, as shown in Fig. S10.† The segregated microdots on the high-content MA film, which are not necessarily at the grain boundaries, may be directly related to defects during crystal growth as discussed above.[85–87] The diffusion mediated defect can start from these points, where the deformation of the lattice can lead to thermodynamically favorable perovskite photodecomposition.[88–90] Currently, our experiment is resolution limited, however, with higher resolution we would be able to

obtain more information about the segregation nature by distinguishing individual grains within the domain. Overall, these experiments' results are consistent with the impact of thermal degradation discussed above. This is visible in the films processed with FIRA for over 2 s – higher temperatures reached due to prolonged annealing affected the perovskite material's intrinsic thermodynamic stability.[51,53,91]

Finally, we manufactured a champion solar cell with 19.5% power conversion efficiency using the optimal process conditions (*i.e.*, $t_f$), and with one of the most stable screened compositions, $FA_{0.9}Cs_{0.1}PbI_3$, as it can be seen in Fig. S11.† In Fig. S11,† we also show a cross-sectional image of the device with the compactness of the perovskite films and the multilayer cell, made with $FTO/TiO_2$ compact-meso/$FA_{0.9}Cs_{0.1}PbI_3$/Spiro-Ometad/Au as the chosen architecture. The *JV* parameters shown by the device denote an efficient solar cell that is quite similar to other related results reported in the literature with other specific compositions.[12,13,92] However, the little hysteresis

shown can be related to the typical roughness of the perovskite crystal growth, impeding a smoother interface with the hole-transport material. Other phenomena related to the hysteresis of the cell are the photoinduced bulk polarization effect, which can be attributed to the rotational barrier of the cations upon photoexcitation.[92,93] It would be considered for future device correlation studies focusing on reducing defect points rather than material detection.

# 3. Verification for bromide-halide and tin-metal center perovskite compositions

To test the applicability of FIRA to perovskites with different constituents, two additional samples were processed: one replacing iodide with bromide halide, the other replacing lead with tin. The ratio of components and annealing times were based on $FA_{0.9}Cs_{0.1}PbI_3$, which was the most stable sample from
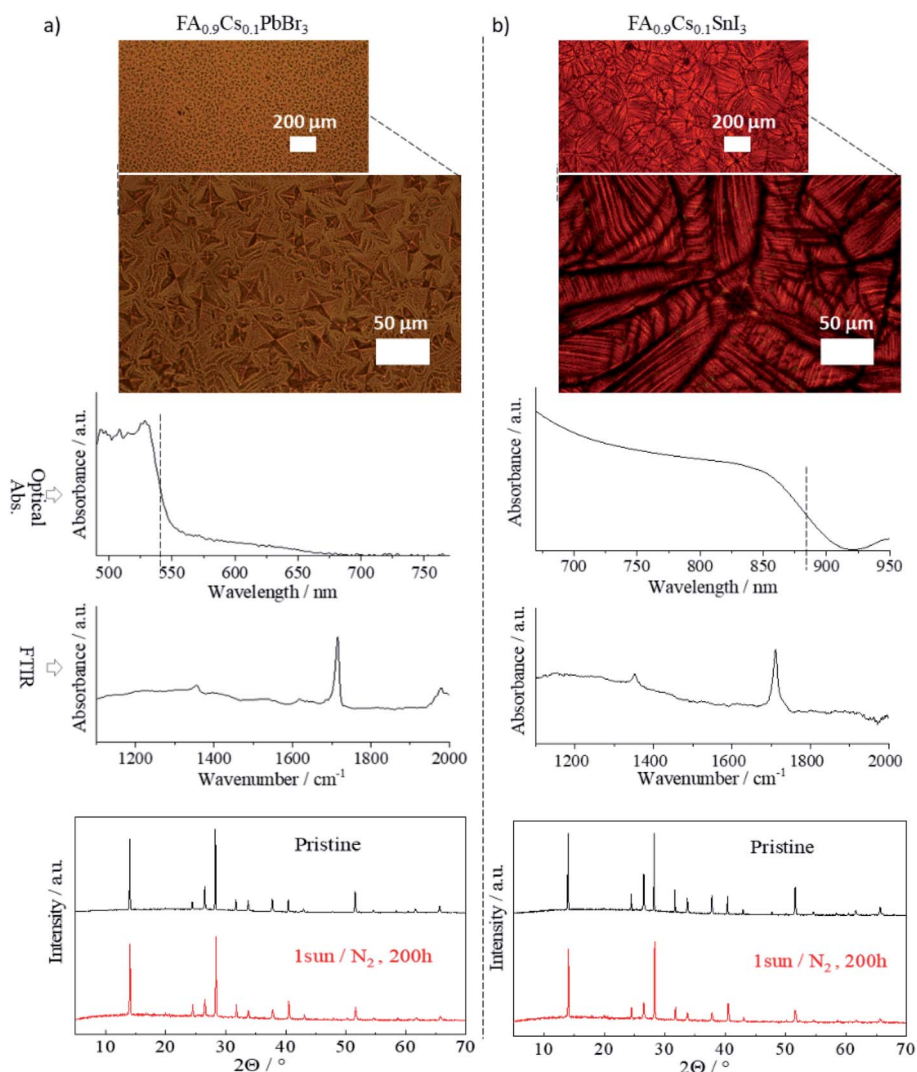


**Fig. 5** Optical image, absorption spectra, FTIR spectra and XRD pattern for (a) $FA_{0.9}Cs_{0.1}PbBr_3$ and (b) $FA_{0.9}Cs_{0.1}SnI_3$ perovskite thin films, annealed at 1.4 s $t_f$.

the original batch. Thus, we annealed $FA_{0.9}Cs_{0.1}PbBr_3$ (FACPB) and $FA_{0.9}Cs_{0.1}SnI_3$ (FACSI) for 1.4 seconds. Optical images of both compositions are shown in Fig. 5. The films are compact with a characteristic oriented growth due to the rapid annealing. However, two different grain arrangements are observed: a microstructured cuboid grain–domain prevails in FACPB, while a spherulitic grain growth is present in FACSI.[49] These different structures point towards different solidification kinetics which depend on various parameters – chemical composition, interface mobility, interfacial energy, and nucleation density, among others – both of which yield compact, gap-free films suitable for manufacturing PSCs.[94,95]

The absorption spectra of both samples are also shown in Fig. 5. The FACPB shows a blue shift while the FACSI is red shifted compared to the $(FAMACs)PbI_3$. Both shifts are expected due to the respective changes to their components. The FTIR spectra of both samples show the characteristic peaks of the C–N antisymmetric stretching vibration at 1713 cm$^{-1}$, which was also seen for the perovskite samples in Fig. 1, with $t_f = 1.4$ s. The XRD pattern of both films also confirms the presence of the perovskite phase in these materials. In both cases, the lattice parameters indicate a pure perovskite with a tetragonal structure (see Fig. S12 and Methods† for lattice parameter calculations). The illumination stress test was performed for both films in the same manner as for the other films. Both showed thermodynamically stable perovskite phases with no presence of secondary phases, as observed in their XRD patterns taken after the stress test. This is especially notable for the Sn-based film; a promising result for low bandgap PSCs advancement.[96,97]

From the combination of the above results, FIRA indeed seems to be an applicable method not just to standard perovskite compositions, but also to novel ones. Moreover, the identified $t_f = 1.4$ s annealing time is almost composition independent. Comparing this to the standard method of using a hot plate, FIRA virtually eliminates annealing time from the overall fabrication time.

# 4. Concluding remarks

Using FIRA to replace traditional annealing methods, and the Thot data framework for data analysis and management, we developed a methodology for fast material screening, providing a database of optical and structural properties for perovskite thin films. Two hundred sixty-six samples were screened based on composition and annealing time, resulting in five that met the structural requirements in terms of perovskite phase formation and thin film stability for future optoelectronic applications. These films are stable due to their cation integration into the perovskite structure. Three different stress tests based on moisture, temperature, and light showed the thermodynamic stability of these samples. We conclude that for the unstable films, photoinduced $PbI_2$ degradation started at defect points that are created during crystal growth. These defects are larger in samples where the cation is not well incorporated into the perovskite lattice. The broad applicability of FIRA was investigated, where controlled photonic pulse annealing leads to highly crystalline perovskite films.

This study aims to create affordable characterization techniques for the solidification of stable, thin-film hybrid perovskite materials. By leveraging large datasets of material characterizations, we expect to find new material properties in these films. The viability of these fundamental studies and commercialization relies on rapid thin film processing methods for data production and material properties screening.

# 5. Experimental methods

### 5.1. Electrodes preparation

For TCO electrodes were used FTO coated glass (Pilkington NSG TEC). The substrates were cleaned with Hellmanex soap, followed by 30 min sonication in a Hellmanex 2% water solution, 15 min sonication in IPA, and 5 min of oxygen plasma etching.

### 5.2. Perovskite solution preparation

The organic salts were purchased from Greatcell; the lead and tin compounds were purchased from TCI. The hybrid perovskite precursor solutions were deposited from a precursor solution containing $CH_5N_2I$, $CH_5N_2Br$, $PbI_2$ and $SnI_2$ (1.4 M), in anhydrous DMF/DMSO 3 : 1 (v/v).

### 5.3. FIRA method

The films made by the FIRA method include the spin-coating of the perovskite solution in a single step at 4000 rpm for 10 s. The substrates were then IR irradiated for different flash times (from 0.2 s to 3.6 s) in the FIRA oven and were kept there for 10 additional seconds before removal. FIRA processing was carried out in a glovebox with $N_2$ atmosphere. The FIRA engineering setup is reported elsewhere.[15,16]

### 5.4. Material characterization

Scanning electron microscopy was carried out on a Tescan MIRA 3 LMH with a field emission source operated at an acceleration voltage of 10 kV. Film X-ray diffraction was performed in reflection spin mode with an Empyrean system (Theta–Theta, 240 mm) equipped with a PIXcel-1D detector, Bragg–Brentano beam optics (including hybrid monochromator), and parallel beam optics. Optical transmission measurements were performed using a Zeiss Axio-Scope A1 Pol using a Zeiss EC Epiplan-Apochromat 10× objective and a xenon light source (Ocean Optics HPX-2000). For spectroscopic measurements, an optical fiber (QP230-2-XSR, 230 μm core) collected the transmitted light from the sample. The spectra were recorded by a spectrometer (Ocean Optics Maya2000 Pro). All spectra were obtained at room temperature in transmission. FTIR was performed with the FTS 7000 spectrometer Digilab, use a He–Ne laser operating at 632.8 nm with an MCT detector for mid-IR measurements and an 896b interferometer. The real panel of the spectrometer is connected for a far-IR power source, an external source, purged air and water coolant. For surface temperature measurement was used a thermocamera FLUKE, with CCD and laser point integrated. The TRPL spectra was measured on a LifeSpec II with a 506 nm excitation wavelength and stopping at $10^4$ counts.

**26892** | *J. Mater. Chem. A*, 2021, **9**, 26885–26895

This journal is © The Royal Society of Chemistry 2021

### 5.5. Lattice parameters calculation

Data were fitted with the Le Bail method using Topas 5. The zero-shift of the detector was previously determined using a standard, and the vertical sample displacement was refined along with the background. A separate set of refinements (not shown here) was done fixing displacement parameters and yielded identical results within e.s.d.'s.

### 5.6. Data processing

The goal of this work was to create a rapid screening methodology for perovskite solar cells. This was achieved using FIRA for fabrication, and the Thot data management and analysis framework (https://pypi.org/project/thot-data/) to process the experimental data. Thot uses a project tree to organize your data, and runs analysis scripts on designated nodes of the tree. Using this framework we created analysis scripts that first analyze the XRD spectrum for the phase ratios and assign the sample classification. The phase classifications are then compared by composition and time.

Thot allowed us to keep our analysis modular. This was greatly useful as adding additional analysis to our project as new questions emerged was made very easy. New data was also easily integrated into the project.

## Conflicts of interest

There are no conflicts to declare.

## References

1 G. Kim, et al., Impact of strain relaxation on performance of α-formamidinium lead iodide perovskite solar cells, Science, 2020, 370, 108–112.

2 M. Jeong, et al., Stable perovskite solar cells with efficiency exceeding 24.8% and 0.3-V voltage loss, Science, 2020, 369, 1615–1620.

3 E.-C. Cho and H.-S. Lee, High-Efficiency Crystalline Silicon Solar Cells, MDPI, 2021.

4 A. Reinders, P. Verlinden, W. van Sark and A. Freundlich, Photovoltaic Solar Energy: from Fundamentals to Applications, John Wiley & Sons, 2017.

5 Westinghouse Electric Corporation, Research & Development Center, Heterostructure Single Crystal Silicon Photovoltaic Solar Cells, 1978.

6 S. Mishra, S. Ghosh and T. Singh, Progress in Materials Development for Flexible Perovskite Solar Cells and Future Prospects, ChemSusChem, 2021, 14, 512–538.

7 H. Li and W. Zhang, Perovskite Tandem Solar Cells: From Fundamentals to Commercial Deployment, Chem. Rev., 2020, 120, 9835–9950.

8 K. Fu, A. W. Ho-Baillie, H. K. Mulmudi and P. T. T. Trang, Perovskite Solar Cells: Technology and Practices, CRC Press, 2019.

9 M. Workman, D. Z. Chen and S. M. Musa, Machine Learning for Predicting Perovskite Solar Cell Opto-Electronic Properties, 2020 International Conference on Data Analytics for Business and Industry: Way towards a Sustainable Economy ICDABI, 2020, DOI: 10.1109/icdabi51230.2020.9325629.

10 T. Chen, Y. Zhou and M. Rafailovich, Application of Machine Learning in Perovskite Solar Cell Crystal Size Distribution Analysis, MRS Adv., 2019, 4, 793–800.

11 B. Yılmaz and R. Yıldırım, Critical review of machine learning applications in perovskite solar research, Nano Energy, 2021, 80, 105546.

12 S. Sánchez, J. Jerónimo-Rendon, M. Saliba and A. Hagfeldt, Highly efficient and rapid manufactured perovskite solar cells via Flash InfraRed Annealing, Mater. Today, 2020, 9–15.

13 S. Sánchez, M. Vallés-Pelarda and J. A. Alberola-Borràs, Flash infrared annealing as a cost-effective and low environmental impact processing method for planar perovskite solar cells, Mater. Today, 2019, 39–46.

14 S. Sanchez, N. Christoph and B. Grobety, Efficient and Stable Inorganic Perovskite Solar Cells Manufactured by Pulsed Flash Infrared Annealing, Adv. Energy Mater., 2018, 1802060.

15 S. Sanchez, X. Hua and A. Guenzler, Flash infrared pulse time control of perovskite crystal nucleation and growth from solution, Cryst. Growth Des., 2020, 670–679.

16 P. S. V. Ling, A. Hagfeldt and S. Sanchez, Flash Infrared Annealing for Perovskite Solar Cell Processing, J. Visualized Exp., 2021, e61730.

17 H. Uratani, C.-P. Chou and H. Nakai, Quantum Mechanical Molecular Dynamics Simulations of Polaron Formation in a Perovskite Solar Cell Material, J. Comput. Chem., Jpn., 2019, 18, 142–144.

18 P. H. Joshi, Understanding the photostability of perovskite solar cell, DOI: 10.31274/etd-180810-5360.

19 J. M. Frost, L. D. Whalley and A. Walsh, Slow Cooling of Hot Polarons in Halide Perovskite Solar Cells, ACS Energy Lett., 2017, 2, 2647–2652.

20 M. C. Brennan, S. Draguta, P. V. Kamat and M. Kuno, Light-induced anion phase segregation in mixed Halide perovskites, ACS Energy Lett., 2018, 3, 204–213.

21 M. Park, et al., Excited-state vibrational dynamics toward the polaron in methylammonium lead iodide perovskite, Nat. Commun., 2018, 9, 2525.

22 F. Zheng and L.-W. Wang, Large polaron formation and its effect on electron transport in hybrid perovskites, Energy Environ. Sci., 2019, 12, 1219–1230.

23 D. Meggiolaro, F. Ambrosio, E. Mosconi, A. Mahata and F. De Angelis, Polarons in metal Halide perovskites, Adv. Energy Mater., 2020, 10, 1902748.

24 L. Zhou, et al., Cation Alloying Delocalizes Polarons in Lead Halide Perovskites, J. Phys. Chem. Lett., 2019, 10, 3516–3524.

25 A. Senocrate, G. Y. Kim, M. Grätzel and J. Maier, Thermochemical stability of hybrid Halide perovskites, ACS Energy Lett., 2019, 4, 2859–2870.

26 E. T. Hoke, et al., Reversible photo-induced trap formation in mixed-halide hybrid perovskites for photovoltaics, Chem. Sci., 2015, 6, 613–617.

27 D. J. Slotcavage, H. I. Karunadasa and M. D. McGehee, Light-induced phase segregation in Halide-perovskite absorbers, ACS Energy Lett., 2016, 1, 1199–1205.

This journal is © The Royal Society of Chemistry 2021

J. Mater. Chem. A, 2021, 9, 26885–26895 | 26893

28 D. T. Limmer and N. S. Ginsberg, Photoinduced phase separation in the lead halides is a polaronic effect, *J. Chem. Phys.*, 2020, **152**, 230901.

29 C. G. Bischak, *et al.*, Origin of Reversible Photoinduced Phase Separation in Hybrid Perovskites, *Nano Lett.*, 2017, **17**, 1028–1033.

30 A. J. Knight, A. D. Wright, J. B. Patel, D. P. McMeekin, H. J. Snaith and M. B. Johnston, *ACS Energy Lett.*, 2019, **4**(1), 75–84.

31 Y. Liu, *et al.*, Inch-sized high-quality perovskite single crystals by suppressing phase segregation for light-powered integrated circuits, *Sci. Adv.*, 2021, **7**, eabc8844.

32 M. A. Hope, *et al.*, Nanoscale Phase Segregation in Supramolecular π-Templating for Hybrid Perovskite Photovoltaics from NMR Crystallography, *J. Am. Chem. Soc.*, 2021, **143**, 1529–1538.

33 J. Liang, *et al.*, Suppressing the Phase Segregation with Potassium for Highly Efficient and Photostable Inverted Wide-Band Gap Halide Perovskite Solar Cells, *ACS Appl. Mater. Interfaces*, 2020, **12**, 48458–48466.

34 I. Mora-Seró Phase Segregation in Perovskite Nanoparticles and Applications of these Materials in Photocatalytic Processes, *Proceedings of the nanoGe Fall Meeting 2019*, 2019, DOI: 10.29363/nanoge.ngfm.2019.176.

35 A. F. Gualdrón-Reyes, S. J. Yoon and I. Mora-Seró, Recent insights for achieving mixed halide perovskites without halide segregation, *Curr. Opin. Electrochem.*, 2018, **11**, 84–90.

36 J. He, W.-H. Fang, R. Long and O. V. Prezhdo, Increased lattice stiffness suppresses nonradiative charge recombination in MAPbI$_3$ doped with larger cations: Time-domain *ab initio* analysis, *ACS Energy Lett.*, 2018, **3**, 2070–2076.

37 R. E. Beal, *et al.*, Structural origins of light-induced phase segregation in organic–inorganic Halide perovskite photovoltaic materials, *Matter*, 2020, **2**, 207–219.

38 H. Funk, *et al.*, *In situ* TEM Monitoring of Phase-Segregation in Inorganic Mixed Halide Perovskite, *J. Phys. Chem. Lett.*, 2020, **11**, 4945–4950.

39 Ruf and Fabian, *Excitonic Effects and Bandgap Instabilities in Perovskite Solar Cells*, KIT Scientific Publishing, 2020.

40 X. Yin, *et al.*, Photoinduced Phase Segregation Leading to Evident Open-Circuit Voltage Loss in Efficient Inorganic CsPbIBr Solar Cells, *J. Phys. Chem. Lett.*, 2020, **11**, 7035–7041.

41 R. Szostak, *et al.*, Revealing the perovskite film formation using the gas quenching method by *in situ* GIWAXS: Morphology, properties, and device performance, *Adv. Funct. Mater.*, 2021, **31**, 2007473.

42 S. Sánchez, L. Pfeifer, N. Vlachopoulos and A. Hagfeldt, Rapid hybrid perovskite film crystallization from solution, *Chem. Soc. Rev.*, 2021, **50**(12), 7108–7131.

43 R. M. Williams and R. Brakkee, Minimizing Defect States in Lead Halide Perovskite Solar Cell Materials, *Appl. Sci.*, 2020, **10**, 3061.

44 A. J. Barker, A. Sadhanala, F. Deschler, M. Gandini, S. P. Senanayak, P. M. Pearce, E. Mosconi, A. J. Pearson, Y. Wu, A. R. S. Kandada, T. Leijtens, F. De Angelis,

S. E. Dutton, A. Petrozza and R. H. Friend, *ACS Energy Lett.*, 2017, **2**(6), 1416–1424.

45 D. Barboni and R. A. De Souza, The thermodynamics and kinetics of iodine vacancies in the hybrid perovskite methylammonium lead iodide, *Energy Environ. Sci.*, 2018, **11**, 3266–3274.

46 N. S. Arul and V. D. Nithya, *Revolution of Perovskite: Synthesis, Properties and Applications*, Springer Nature, 2020.

47 M. Pazoki, A. Hagfeldt and T. Edvinsson, *Characterization Techniques for Perovskite Solar Cell Materials*, Elsevier, 2019.

48 J. C. Brauer, *et al.*, Comparing the excited-state properties of a mixed-cation-mixed-halide perovskite to methylammonium lead iodide, *J. Chem. Phys.*, 2020, **152**, 104703.

49 L. A. Muscarella, *et al.*, Crystal Orientation and Grain Size: Do They Determine Optoelectronic Properties of MAPbI$_3$ Perovskite?, *J. Phys. Chem. Lett.*, 2019, **10**, 6010–6018.

50 V. Adinolfi, W. Peng, G. Walters, O. M. Bakr and E. H. Sargent, The Electrical and Optical Properties of Organometal Halide Perovskites Relevant to Optoelectronic Performance, *Adv. Mater.*, 2018, **30**, 1700764.

51 S. Kim, *et al.*, Relationship between ion migration and interfacial degradation of CHNHPbI perovskite solar cells under thermal conditions, *Sci. Rep.*, 2017, **7**, 1200.

52 O. R. Yamilova, A. V. Danilov, M. Mangrulkar, Y. S. Fedotov, S. Yu. Luchkin, S. D. Babenko, S. I. Bredikhin, S. M. Aldoshin, K. J. Stevenson and P. A. Troshin, *J. Phys. Chem. Lett.*, 2020, **11**(1), 221–228.

53 Z. Ahmad, *et al.*, Degradation analysis in mixed (MAPbI$_3$ and MAPbBr$_3$) perovskite solar cells under thermal stress, *J. Mater. Sci.: Mater. Electron.*, 2019, **30**, 1354–1359.

54 V. C. A. Taylor, *et al.*, Investigating the Role of the Organic Cation in Formamidinium Lead Iodide Perovskite Using Ultrafast Spectroscopy, *J. Phys. Chem. Lett.*, 2018, **9**, 895–901.

55 S. Maheshwari, M. B. Fridriksson, S. Seal, J. Meyer and F. C. Grozema, The Relation between Rotational Dynamics of the Organic Cation and Phase Transitions in Hybrid Halide Perovskites, *J. Phys. Chem. C*, 2019, **123**, 14652–14661.

56 M. T. Weller, O. J. Weber, J. M. Frost and A. Walsh, Cubic perovskite structure of black formamidinium lead iodide, α-[HC(NH$_2$)$_2$]PbI$_3$, at 298 K, *J. Phys. Chem. Lett.*, 2015, **6**, 3209–3212.

57 F. Ma, *et al.*, Stable α/δ phase junction of formamidinium lead iodide perovskites for enhanced near-infrared emission, *Chem. Sci.*, 2017, **8**, 800–805.

58 X. Guo, *et al.*, Identification and characterization of the intermediate phase in hybrid organic–inorganic MAPbI$_3$ perovskite, *Dalton Trans.*, 2016, **45**, 3806–3813.

59 I. Khan *et al.*, *Hybrid Perovskite Composite Materials: Design to Applications*, Woodhead Publishing, 2020.

60 W. Zhang, *Metal Halide Perovskite Crystals: Growth Techniques, Properties and Emerging Applications*, MDPI, 2019.

61 M. I. Ustinova, *et al.*, Partial Substitution of Pb in CsPbI as an Efficient Strategy To Design Fairly Stable All-Inorganic Perovskite Formulations, *ACS Appl. Mater. Interfaces*, 2021, **13**, 5184–5194.

26894 | *J. Mater. Chem. A*, 2021, **9**, 26885–26895

This journal is © The Royal Society of Chemistry 2021

62 J. Zhang, *et al.*, Improved phase stability of the CsPbI perovskite via organic cation doping, *Phys. Chem. Chem. Phys.*, 2019, **21**, 11175–11180.

63 Y.-Z. Wang, *et al.*, A-site cation with high vibrational motion in ABX perovskite effectively induces dielectric phase transition, *Dalton Trans.*, 2021, **50**, 3841–3847.

64 A. Singh, M. K. Jana and D. B. Mitzi, Reversible Crystal-Glass Transition in a Metal Halide Perovskite, *Adv. Mater.*, 2021, **33**, e2005868.

65 S. Sanchez, X. Hua, N. Phung and U. Steiner, Flash Infrared Annealing for Antisolvent-Free Highly Efficient Perovskite Solar Cells, *Adv. Energy Mater.*, 2018, **8**, 1702915.

66 D. J. Kubicki, *et al.*, Phase Segregation in Cs-, Rb- and K-Doped Mixed-Cation (MA)(FA)PbI Hybrid Perovskites from Solid-State NMR, *J. Am. Chem. Soc.*, 2017, **139**, 14173–14180.

67 X. Liu, *et al.*, Highly Stable New Organic-Inorganic Hybrid 3D Perovskite CHNHPdI and 2D Perovskite (CHNH)PdI: DFT Analysis, Synthesis, Structure, Transition Behavior, and Physical Properties, *J. Phys. Chem. Lett.*, 2018, **9**, 5862–5872.

68 W. A. Saidi and J. J. Choi, Nature of the cubic to tetragonal phase transition in methylammonium lead iodide perovskite, *J. Chem. Phys.*, 2016, **145**, 144702.

69 Y. Liu, *et al.*, Stabilization of Highly Efficient and Stable Phase-Pure FAPbI Perovskite Solar Cells by Molecularly Tailored 2D-Overlayers, *Angew. Chem., Int. Ed. Engl.*, 2020, **59**, 15688–15694.

70 Y. Yamada, T. Yamada and Y. Kanemitsu, Free carrier radiative recombination and photon recycling in lead Halide perovskite solar cell materials, *Bull. Chem. Soc. Jpn.*, 2017, **90**, 1129–1140.

71 M. Stolterfoht, *et al.*, Visualization and suppression of interfacial recombination for high-efficiency large-area pin perovskite solar cells, *Nat. Energy*, 2018, **3**, 847–854.

72 Z. Chen, *et al.*, Methylammonium, formamidinium and ethylenediamine mixed triple-cation perovskite solar cells with high efficiency and remarkable stability, *J. Mater. Chem. A*, 2018, **6**, 17625–17632.

73 C. G. Bischak, *et al.*, Tunable Polaron Distortions Control the Extent of Halide Demixing in Lead Halide Perovskites, *J. Phys. Chem. Lett.*, 2018, **9**, 3998–4005.

74 M. Delor, *et al.*, Carrier diffusion lengths exceeding 1 μm despite trap-limited transport in Halide double perovskites, *ACS Energy Lett.*, 2020, **5**, 1337–1345.

75 A. J. Neukirch, *et al.*, Geometry Distortion and Small Polaron Binding Energy Changes with Ionic Substitution in Halide Perovskites, *J. Phys. Chem. Lett.*, 2018, **9**, 7130–7136.

76 https://arxiv.org/pdf/2012.05115.pdf.

77 A. J. Neukirch, *et al.*, Polaron Stabilization by Cooperative Lattice Distortion and Cation Rotations in Hybrid Perovskite Materials, *Nano Lett.*, 2016, **16**, 3809–3816.

78 S. Stranks, Visualising the Impact of Defects and Strain on Halide Perovskite Structures, *Proceedings of the 11th International Conference on Hybrid and Organic Photovoltaics*, 2019, DOI: 10.29363/nanoge.hopv.2019.058.

79 H.-G. Duan, *et al.*, Photoinduced Vibrations Drive Ultrafast Structural Distortion in Lead Halide Perovskite, *J. Am. Chem. Soc.*, 2020, **142**, 16569–16578.

80 Y. Lan, *et al.*, Ultrafast correlated charge and lattice motion in a hybrid metal halide perovskite, *Sci. Adv.*, 2019, **5**, eaaw5558.

81 R. A. Scheidt and P. V. Kamat, Temperature-driven anion migration in gradient halide perovskites, *J. Chem. Phys.*, 2019, **151**, 134703.

82 M. C. Brennan, A. Ruth, P. V. Kamat and M. Kuno, Photoinduced anion segregation in mixed Halide perovskites, *Trends Chem.*, 2020, **2**, 282–301.

83 T. Elmelund, B. Seger, M. Kuno and P. V. Kamat, How interplay between photo and thermal activation dictates Halide ion segregation in mixed Halide perovskites, *ACS Energy Lett.*, 2020, **5**, 56–63.

84 W. Jian, R. Jia, H.-X. Zhang and F.-Q. Bai, Arranging strategies for A-site cations: impact on the stability and carrier migration of hybrid perovskite materials, *Inorg. Chem. Front.*, 2020, **7**, 1741–1749.

85 J.-W. Lee, *et al.*, Solid-phase hetero epitaxial growth of α-phase formamidinium perovskite, *Nat. Commun.*, 2020, **11**, 5514.

86 Y. Lv, *et al.*, All-in-One Deposition to Synergistically Manipulate Perovskite Growth for High-Performance Solar Cell, *Research*, 2020, **2020**, 2763409.

87 N. F. DeMarco, *Defect and Grain Boundary Engineering for Enhanced Performances and Lifetimes of Hybrid Perovskite Solar Cells*, 2019.

88 D. O. Tiede, M. E. Calvo, J. F. Galisteo-López and H. Míguez, Local Rearrangement of the Iodide Defect Structure Determines the Phase Segregation Effect in Mixed-Halide Perovskites, *J. Phys. Chem. Lett.*, 2020, **11**, 4911–4916.

89 M. V. Khenkin, *et al.*, Dynamics of photoinduced degradation of perovskite photovoltaics: From reversible to irreversible processes, *ACS Appl. Energy Mater.*, 2018, **1**, 799–806.

90 T. W. Jones, *et al.*, Lattice strain causes non-radiative losses in halide perovskites, *Energy Environ. Sci.*, 2019, **12**, 596–606.

91 M. A. Green, A. Ho-Baillie and H. J. Snaith, The emergence of perovskite solar cells, *Nat. Photonics*, 2014, **8**, 506–514.

92 Y. Zhao, W. Zhou, Z. Han, D. Yu and Q. Zhao, Effects of ion migration and improvement strategies for the operational stability of perovskite solar cells, *Phys. Chem. Chem. Phys.*, 2021, **23**, 94–106.

93 T. Wu, *et al.*, Photoinduced Bulk Polarization and Its Effects on Photovoltaic Actions in Perovskite Solar Cells, *ACS Nano*, 2017, **11**, 11542–11549.

94 K. Wang, *et al.*, Kinetic Stabilization of the Sol-Gel State in Perovskites Enables Facile Processing of High-Efficiency Solar Cells, *Adv. Mater.*, 2019, **31**, e1808357.

95 X. Zhang, *et al.*, Phase Transition Control for High Performance Ruddlesden-Popper Perovskite Solar Cells, *Adv. Mater.*, 2018, **30**, e1707166.

96 Z. Zhu, C.-C. Chueh, N. Li, C. Mao and A. K.-Y. Jen, Realizing Efficient Lead-Free Formamidinium Tin Triiodide Perovskite Solar Cells via a Sequential Deposition Route, *Adv. Mater.*, 2018, **30**, 1703800.

97 G. Liu, *et al.*, Regulated Crystallization of Efficient and Stable Tin-Based Perovskite Solar Cells via a Self-Sealing Polymer, *ACS Appl. Mater. Interfaces*, 2020, **12**, 14049–14056.

This journal is © The Royal Society of Chemistry 2021

*J. Mater. Chem. A*, 2021, **9**, 26885–26895 | **26895**